

Probing subcycle spectral structures and dynamics of high-order harmonic generation in crystals

Long Lin(林龙), Tong-Gang Jia(贾铜钢), Zhi-Bin Wang(王志斌), and Peng-Cheng Li(李鹏程)
Citation: Chin. Phys. B, 2022, 31 (**9**): 093202. DOI: 10.1088/1674-1056/ac6943
Journal homepage: http://cpb.iphy.ac.cn; http://iopscience.iop.org/cpb

What follows is a list of articles you may be interested in

Generation of elliptical isolated attosecond pulse from oriented H_2^+ in a linearly polarized laser field

Yun-He Xing(邢云鹤), Jun Zhang(张军), Xiao-Xin Huo(霍晓鑫), Qing-Yun Xu(徐清芸), and Xue-Shen Liu(刘学深)
Chin. Phys. B, 2022, 31 (**4**): 043203. DOI: 10.1088/1674-1056/ac398b

Generation of non-integer high-order harmonics and significant enhancement of harmonic intensity

Chang-Long Xia(夏昌龙), Yue-Yue Lan(兰悦跃), and Xiang-Yang Miao(苗向阳)
Chin. Phys. B, 2021, 30 (**4**): 043202. DOI: 10.1088/1674-1056/abd389

Multiphoton quantum dynamics of many-electron atomic and molecular systems in intense laser fields

Peng-Cheng Li(李鹏程), Shih-I Chu
Chin. Phys. B, 2020, 29 (**8**): 083202. DOI: 10.1088/1674-1056/ab9c0f

Role of potential on high-order harmonic generation from atoms irradiated by bichromatic counter-rotating circularly polarized laser fields

Xu-Xu Shen(申许许), Jun Wang(王俊), Fu-Ming Guo(郭福明), Ji-Gen Chen(陈基根), Yun-Jun Yang(杨玉军)
Chin. Phys. B, 2020, 29 (**8**): 083201. DOI: 10.1088/1674-1056/ab961c

Semi-integer harmonic generation from an argon atom by bichromatic counter-rotating circularly polarized laser field

Tong Qi(齐桐), Xiao-Xin Huo(霍晓鑫), Jun Zhang(张军), Xue-Shen Liu(刘学深)
Chin. Phys. B, 2020, 29 (**5**): 053201. DOI: 10.1088/1674-1056/ab821b

---

Probing subcycle spectral structures and dynamics of high-order harmonic generation in crystals

Long Lin(林龙)[1,2], Tong-Gang Jia(贾铜钢)[1,2], Zhi-Bin Wang(王志斌)[3], and Peng-Cheng Li(李鹏程)[1,2,†]

[1] *Research Center for Advanced Optics and Photoelectronics, Department of Physics, College of Science, Shantou University, Shantou* 515063, *China*
[2] *Key Laboratory of Intelligent Manufacturing Technology of MOE, Shantou University, Shantou* 515063, *China*
[3] *College of Physics and Electronic Engineering, Northwest Normal University, Lanzhou* 730070, *China*

(Received 11 February 2022; revised manuscript received 19 April 2022; accepted manuscript online 22 April 2022)

Subcycle spectral structures and dynamics of high-order harmonic generation (HHG) processes of atoms and molecules driven by intense laser fields on the attosecond time scale have been originally studied theoretically and experimentally. However, the time scale of HHG dynamics in crystals is in the order of sub-femtosecond, and the carrier dynamics of HHG in crystals driven by subcycle laser pulses are largely unexplored. Here we perform a theoretical study of subcycle structures, spectra, and dynamics of HHG of crystals in mid-infrared laser fields subject to excitation by a subcycle laser pulse with a time delay. The HHG spectra as a function of time delay between two laser fields are calculated by using a single-band model for the intra-band carrier dynamics in crystal momentum space and by solving the time-dependent Schrödinger equation in velocity gauge for the treatment of multi-band crystal systems. The results exhibit a complex time-delay-dependent oscillatory pattern, and the enhancement and suppression of the HHG related to subcycle pulse are observed at the given time delay in either single-band or multi-band crystal systems. To understand oscillation structures with respect to the dependence for the subcycle laser fields, the time-frequency characteristics of the HHG as well as the probability density distribution of the radiation are analyzed in detail.

Keywords: high-order harmonic generation, carrier dynamics, subcycle laser pulses, crystal systems

PACS: 32.80.Rm, 42.65.Ky, 42.50.Hz, 42.65.Re **DOI:** 10.1088/1674-1056/ac6943

1. Introduction

High-order harmonic generation (HHG) caused by the intense ultrafast laser fields[1–7] has been one of the hottest topics in modern ultrafast physics since one of the promising methods for generation of attosecond pulses. The structural and electronic dynamic information of a system is carried by the HHG spectra and momentum spectroscopy,[8–10] which have a very important application in direct imaging material structure and electronic trajectory.[11,12] In particular, the HHG in crystals is a subject of much current interest, which is related to new phenomena and electron dynamics.[13–17] Since the experimental observation of non-perturbative crystal harmonics passed through lasers operating in the mid-infrared (MIR) scale,[18] the emergence of HHG in crystals has attracted extensive attention in the field of attosecond science. Extending the success of attosecond metrology in the gas phase to crystal systems can help us to obtain new compact ultrafast light sources.[19–23] The harmonic generation mechanism in crystals is different from the gas phase owing to the high density and periodicity of crystals.[18]

Currently, there are more and more fundamental studies about HHG in crystals. The experiments by Schubert *et al.*[24] have proved that subcycle electron dynamics play an important role in the crystal-state harmonic generation by revealing the carrier-envelope phase dependence in the harmonic spectrum of GaSe crystal driven by strong field of 30 THz. Vampa *et al.*[25] have proposed a method to apply gas-phase high-harmonic spectroscopy to crystals, which can be explained by classical trajectory analysis. The effects of impurities and scattering of harmonic generation in crystals have been investigated by Kemper *et al.*[26] Fu *et al.*[27] theoretically investigated the dynamic processes of solid harmonics generation using the one-dimensional time-dependent density functional theory. To date, it is generally accepted that the HHG in crystals is contributed by two distinct mechanisms: intra-band current and inter-band polarization. Wu *et al.*[28] have explained in detail that the multi-plateau structures of HHG in crystals are related to these mechanisms. Li *et al.*[29] have studied the enhancement of the second plateau in solid high-order harmonic spectra by two-color fields. The inter-band transitions are analogous to the three-step model in gas HHG. To gain insight into the physical dynamics underlying extreme ultraviolet (XUV) emission in experiments, Luu *et al.*[19] have conducted both semiclassical mechanical simulations and verified the consistency of the single-band model to experimental results. Their results have proved that the laser-driven intra-band current can accurately capture the XUV emission. In addition, it constitutes the first measurement of the fine details of the conduction band dispersion in wide band-gap materials. The study of dielectric materials, especially wide bandgap materials, has broad theoretical and application prospects. Chen *et*

†Corresponding author. E-mail: pchli@stu.edu.cn

© 2022 Chinese Physical Society and IOP Publishing Ltd

al.[30] have investigated probing dynamic information and spatial structure of Rydberg wave packets by harmonic spectra in a few-cycle laser pulse. They explained the harmonic spectra with a periodic variation, which directly illustrates the electron oscillation between the two neighboring Rydberg states by controlling the time delay of pump-probe laser pulses.

Because of the carrier motion in crystals, which can make almost the instantaneous response to the perturbing laser field, subcycle spectral structures and dynamics of HHG processes can be uncovered by probing the transient changes of the carrier by adding the few-cycle laser pulses to the fundamental laser field. The subcycle HHG is theoretically very well understood in atom[31–35] and molecule systems. Chini *et al.*[32] have studied the subcycle AC stark shifts in helium atoms on the attosecond time scale. Subcycle dynamics have been revealed by Bell and Chen,[33] who have carried out the transient absorption XUV spectroscopy experiments on helium in the presence of near-infrared laser fields. Considering the electron correlation, electronic dynamical response and laser polarization effects, Heslar *et al.*[34,35] have analyzed the several subcycle dynamical behaviors of the energy level spectrum and fine structures of the photoemission line patterns in two-color two-photon processes. However, the HHG in crystals driven by the subcycle laser pulses is less understood. The goal of this work is to understand the subcycle spectral structure and dynamical process of the HHG in crystals. Here, we adopt Luu's model for probing subcycle spectral structures and dynamics of intra-band HHG in crystals. The same scheme has been extended for probing the oscillation structures of multi-band from the practically mixed intra- and inter-band crystalline HHG spectrum based on Bloch state basis.[36] HHG in crystals creates a new methodology to understand all-optical spectroscopy of the current carrier structure and dynamics in crystals.

In this paper, we present the HHG spectra of crystals in MIR laser fields and the few-cycle femtosecond laser pulse with a time delay. The HHG spectra of crystals are calculated by solving the Boltzmann equation in crystal momentum space for the intra-band carrier dynamics and the time-dependent Schrödinger equation (TDSE) based on Bloch state basis in velocity gauge for the treatment of multi-band crystal systems. From the HHG spectra as a function of time delay, it is seen that oscillation structures are similar to both single-band and multi-band crystal systems, but it is different from the atomic and molecular systems. Combining the spectral and temporal spectra and the probability density distribution of the radiation in crystal momentum space, subcycle spectral structures, and dynamics of the HHG in crystals are clarified.

2. Theoretical methods

2.1. Single-band model

The HHG spectra can be obtained by performing a calculation of the Boltzmann equation in crystal momentum space for the intra-band carrier dynamics and the TDSE based on Bloch state basis in velocity gauge for the treatment of multi-band crystal systems, respectively.

For the one-dimensional single-band model,[37] the Boltzmann equation related to the time evolution of the population distribution $f(k,t)$ can be written as

$$\frac{\mathrm{d}f(k_\mathrm{c},t)}{\mathrm{d}t} = -\frac{q}{\hbar}E(t)\frac{\partial f(k_\mathrm{c},t)}{\partial k}, \tag{1}$$

where $f(k_\mathrm{c},t)$ is a population of the particle at crystal momentum k_c, q is the charge of the particle, and $E(t)$ is the electric field. In this model, the electron is assumed to be excited to the conduction band of the lowest energy at the beginning of the pulse and moves within the same band without further excitation to higher conduction bands or de-excitation to lower valence bands. Despite its simplicity, this model has been shown to give HHG power spectrum that is comparable to experimental results.[19] It is feasible that this model is selected as the basis for subcycle intra-conduction band dynamics of further study of HHG in crystals. We assume that the external fields are polarized in the same direction. The laser fields can be written as

$$E(t) = E_1(t) + E_2(t), \tag{2}$$

where the pumping field can be expressed as

$$E_1(t) = E_{01}\cos^2\left(\frac{\pi}{N_1T_1}t\right)\cos(\omega_1 t), \tag{3}$$

and the probing field can be expressed as

$$E_2(t) = E_{02}\cos^2\left[\frac{\pi}{N_2T_2}(t-t_\mathrm{d})\right]\cos[\omega_2(t-t_\mathrm{d})]. \tag{4}$$

We would propagate a Gaussian packet with a center at k_{c0} and standard deviation σ as

$$f(k_\mathrm{c},t=0) = \frac{1}{\sigma\sqrt{2\pi}}\mathrm{e}^{-\frac{k_\mathrm{c}^2}{2\sigma^2}}. \tag{5}$$

The dispersion relation is generally expanded in the Fourier series. For general symmetric band structure, the band structure $\varepsilon(k_\mathrm{c})$ is assumed to be symmetric about the origin at the crystal momentum $k_\mathrm{c}=0$ and $\varepsilon(k_\mathrm{c}) = \varepsilon(-k_\mathrm{c})$, it can be expressed as

$$\varepsilon(k_\mathrm{c}) = \frac{\hbar^2}{m_\mathrm{e}a^2}\sum_{n=0}^{n_\mathrm{max}} d_n\cos(nak_\mathrm{c}), \tag{6}$$

where m_e is the effective mass of the particle in the single-band, a is the lattice constant, and d_n is the expansion coefficient of the nth component. We set the first Brillouin zone

to be $(-\frac{g}{2}, \frac{g}{2})$ with $g = \frac{2\pi}{a}$, the corresponding current in the conduction band $j(t)$ can be written as

$$J(t) = q\int_{\mathrm{BZ}} v_{\mathrm{g}}(k_{\mathrm{c}}) f(k_{\mathrm{c}},t)\,\mathrm{d}k_{\mathrm{c}}. \tag{7}$$

The group velocity in the single-band can be calculated as

$$v_{\mathrm{g}}(k_{\mathrm{c}}) = \frac{1}{\hbar}\frac{\partial \varepsilon(k_{\mathrm{c}})}{\partial k_{\mathrm{c}}}. \tag{8}$$

In addition, we put the definition of effective mass as follows:

$$m_{\mathrm{e}}(k_{\mathrm{c}}) = \frac{\hbar^2}{\partial^2 \varepsilon(k_{\mathrm{c}})/\partial k_{\mathrm{c}}^2}. \tag{9}$$

The dipole radiation intensity $I(t)$ is proportional to the absolute square of acceleration. Considering the fact that the intra-band current is the particle velocity, the radiation intensity is proportional to the absolute square of changing rate of intra-band current

$$I(t) \propto \left|\frac{\mathrm{d}J(t)}{\mathrm{d}t}\right|^2. \tag{10}$$

In the frequency domain, this relation can be rewritten as[38]

$$I(\omega) \propto |\omega J(\omega)|^2. \tag{11}$$

2.2. Multi-band model

For multi-band crystal systems, the TDSE in velocity gauge is employed based on the Bloch state basis[39] for an electron interacting with a periodic potential as follows:

$$\mathrm{i}\hbar\frac{\partial}{\partial t}|\psi(t)\rangle = \left(\frac{\hat{p}^2}{2m} + V(\hat{x}) + \frac{e}{m}A(t)\hat{p}\right)|\psi(t)\rangle, \tag{12}$$

where $A(t)$ is the vector potential calculated by the dipole approximation $A(x,t) \approx A(t)$ because the wavelengths used are much larger than the lattice constant, and $A(t)$ is related to the electric field by

$$A(t) = -\int_{-\infty}^{t} E(t')\,\mathrm{d}t', \tag{13}$$

$\hat{p}$ is the momentum operator, and $V(x)$ is the periodic lattice potential which can be written as

$$V(x) = -V_0\left[1 + \cos\left(\frac{2\pi x}{a_0}\right)\right], \tag{14}$$

with $V_0 = 0.37$ and lattice constant $a_0 = 8$, both in atomic units. According to Bloch's theorem, each Bloch state can be written as a product of a plane wave and a periodic function:

$$\langle x|\phi_k^n\rangle = \mathrm{e}^{\mathrm{i}kx}U_k^n(x), \tag{15}$$

where $U_k^n(x)$ satisfy $U_k^n(x+a_0) = U_k^n(x)$. For each value of the quasimomentum k, ϕ_k^n is the electron wave function in the basis of Bloch states:

$$|\psi_k(t)\rangle = \sum_n C_k^n(t)|\phi_k^n\rangle, \tag{16}$$

where Bloch states $|\phi_k^n\rangle$ are evaluated by solving the single-electron stationary Schrödinger equation

$$\left[\frac{\hat{p}^2}{2m} + V(x)\right]|\phi_k^n\rangle = \varepsilon_n(k)|\phi_k^n\rangle, \tag{17}$$

where n is the band index and the eigenvalues $\varepsilon_n(k)$ represent the dispersion relations of the bands. The time-dependent laser-induced microscopic current $j(t)$ can be expressed by the sum of the current in each of the different k channels:

$$j(t) = -\frac{e}{m}\int\{\mathrm{Re}[\langle\phi_k|\hat{p}|\psi_k\rangle] + eA(t)\}\,\mathrm{d}k. \tag{18}$$

The HHG spectra can be obtained from the modulus square $|J(\omega)|^2$ of Fourier transform of the time-dependent current in Eq. (18).

3. Results and discussions

3.1. Laser-induced intra-band HHG oscillation structures

3.1.1. Spectral and temporal features of oscillation structures

It is well known that the experimental studies of subcycle AC Stark shifts in atoms have been reported.[30,40–42] To a comprehensive understanding of subcycle spectral structures and dynamics of HHG processes in crystals, one advantage of studying is firstly an exploration of the intra-band carrier contributions. The Boltzmann equation provides complementary information to identify intra-band dynamics of the crystals. Although the Boltzmann equation is at best qualitative, its single-band carrier dynamics provides a clearer physical picture for the HHG in crystals. To understand the generation of HHG oscillation structures in crystals driven by an MIR and subcycle laser pulse with a time delay, Fig. 1 presents the corresponding scheme. It is clearly seen that the oscillatory pattern in HHG spectra becomes much more complex in comparison with the atomic case.[32,34,35,40]

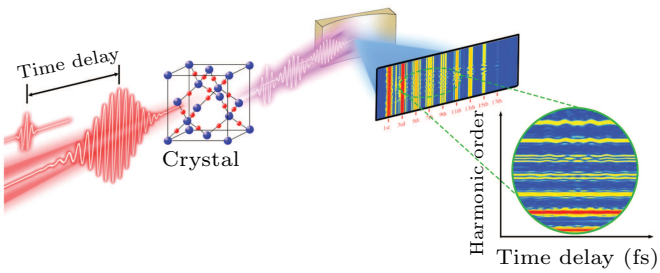


Fig. 1. Schemes of the generation of HHG oscillation structures in crystals driven by the MIR and subcycle laser pulse with a time delay.

Figure 2 presents the oscillating pattern of the HHG of the crystal SiO_2 driven by the MIR laser fields subject to excitation by a subcycle laser pulse. There are obvious shifts between odd orders and various oscillating structures. As shown

in this figure, we have selected two regions where the oscillation structures are quite regular and marked with red dashed circles. In order to further analyze the oscillation structures, we have also selected some relatively representative time delays as shown in Fig. 3. In calculation, we consider a one-dimensional model of the first conduction band of SiO_2 with lattice constant along with Γ–M equal to 0.491 nm. The conduction band structure $\varepsilon(k_c)$ is symmetric concerning the zero crystal momentum $k_c = 0$ and is expanded as a Fourier cosine series by Eq. (6). The significant Fourier expansion coefficients of this conduction band up to the 5th mode are $d_0 = 10.6$, $d_1 = -1.669$, $d_2 = 0.0253$, $d_3 = -0.0098$, $d_4 = 0.0016$, and $d_5 = 0.0263$, with all in units of eV. We set the wavelength λ_1 of the MIR pulse as 2533.1 nm, the duration of the laser pulse is 80.3 fs with a $\cos^2$ envelope. The 2533.1 nm has been chosen for probing subcycle spectral structures and dynamics of intra-band HHG in crystals based on the model band structure we selected. The wavelength λ_2 of the probing pulse is 3800 nm with a 13.8-fs full width at half maximum (FWHM), which just is one third of the energy range of the single-band model. The laser intensities used are $I_1 = 1 \times 10^{12}$ W/cm^2 and $I_2 = 1 \times 10^{10}$ W/cm^2, respectively. I_1 and I_2 are obtained by $|E_{01}|^2$ and $|E_{02}|^2$ as shown in Eqs. (3) and (4). In our calculation, the laser intensity is chosen based on the pervious theoretical or experimental studies.[28] The HHG is calculated as a function of the time delay between two laser pulses, it allows us to understand the carrier dynamics of the HHG in crystals. Here the time delay t_d is in the range -40 fs $\leq t_d \leq 40$ fs. For the intra-band HHG, the carrier moves under the action of the laser field, producing intra-band current and photons emission. The result shows that the oscillating pattern of the HHG becomes more complex in crystals.

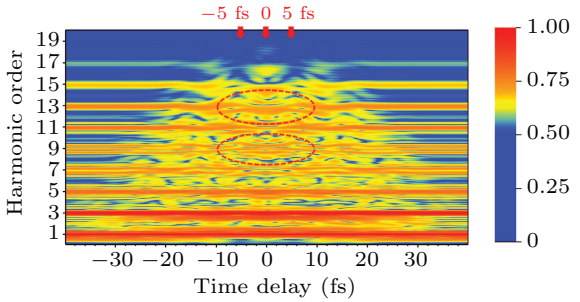


Fig. 2. HHG spectra from SiO_2 as a function of the time delay between MIR and subcycle laser pulses. The red dashed lines indicate the regions of the oscillating pattern.

To further analyze subcycle intra-conduction band dynamics of HHG in crystals, the specific time delay t_d is selected to further investigate the underlying physical mechanisms of these oscillations. We present the HHG spectra with three specific time delays at $t_d = -5$ fs, $t_d = 0$ fs, and $t_d = 5$ fs marked by the red arrows as shown in Fig. 2. The results are shown in Fig. 3. It can be seen that the harmonic spectrum under the monochromatic mid-infrared laser field also has multiple sub-peaks. The reason is that the energy band oscillates with the time-dependent laser field, leading to a temporally changing band structure called the subband.[43] The excitations between the band and subband are responsible for the generation of multiple sub-peaks of harmonic spectra. This phenomenon is similar to the role of the dressed state in the atomic systems. Thus, multiple sub-peaks are generated either MIR-subcycle laser or MIR alone, especially the region of the plateau. It is obvious that HHG spectra have a shift with various time delays.

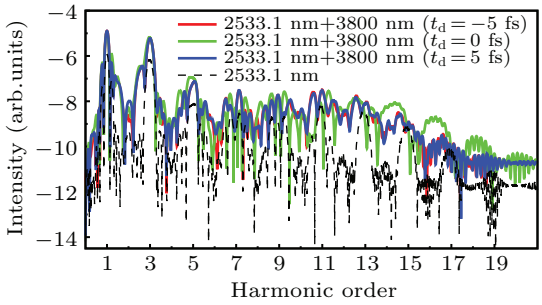


Fig. 3. HHG spectra in MIR and subcycle laser pulses at three specific time delays with $t_d = -5$ fs, $t_d = 0$ fs, and $t_d = 5$ fs, respectively. For comparison, the HHG spectra of the crystal driven by the MIR laser pulse alone are presented as the black dashed line.

To explore the detailed spectral and temporal features of the HHG oscillation structures from crystals, we perform the time-frequency analysis by means of the wavelet transform of the current $J(t)$:

$$A_w(t_0, \omega) = \int J(t) w_{t_0,\omega}(t)\,\mathrm{d}t = d_\omega(t), \tag{19}$$

where $w_{t_0,\omega}(t) = \sqrt{\omega} W(\omega(t - t_0))$. For the harmonic emission, a natural choice of the mother wavelet is given by the Morlet wavelet:

$$W(x) = (1/\sqrt{\tau})\, \mathrm{e}^{\mathrm{i}x}\, \mathrm{e}^{-x^2/2\tau^2}. \tag{20}$$

We choose $\tau = 15$ to perform the wavelet transform. Figures 4(a), 4(b), and 4(c) show the time-frequency spectra of the current in crystals at time delay $t_d = -5$ fs, $t_d = 0$ fs, and $t_d = 5$ fs, respectively. These results reveal striking details of the spectral and temporal structures. As illustrated in this figure, the symmetry of the emission spectra is broken when the time delay shifts from $t_d = -5$ fs to $t_d = 5$ fs, and the shifts of maximum emission energy correspond to the time delays of two pulses.

In Fig. 4(a), the subcycle probing pulse is at the rising edge of the laser field with $t_d = -5$ fs, the maximum energy of HHG emission decreases obviously at this side. However, the maximum energy of HHG emission increases obviously at the same edge with $t_d = 5$ fs. This is the presentation of HHG time-frequency profiles that exhibits the subtle details of spectral and temporal structures for the whole energy range. In addition, in the high energy region, the time-frequency profiles show a netlike structure because only the intra-band harmonics

are considered. Noticeably, it does not show short- and long-trajectories within each optical cycle. The features discussed here are not similar to those observed in the atomic case.

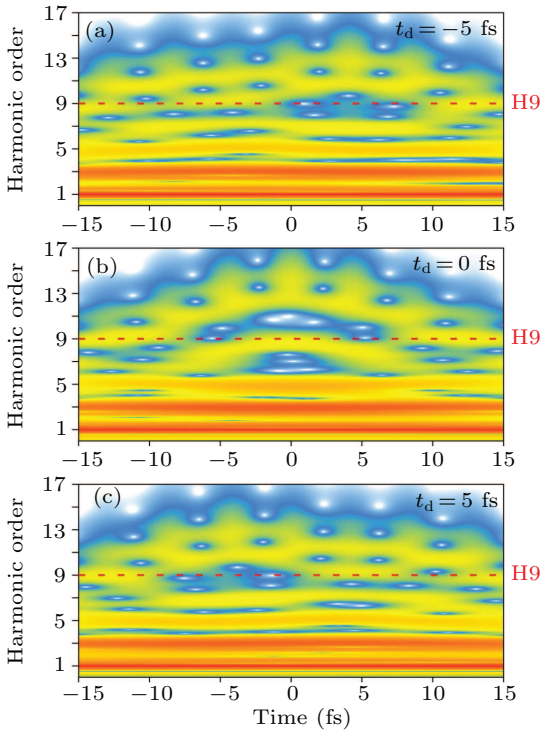


Fig. 4. Wavelet time-frequency spectra of the HHG in crystals: (a) $t_d = -5$ fs, (b) $t_d = 0$ fs, (c) $t_d = 5$ fs, respectively. The laser parameters used are the same as those in Fig. 3.

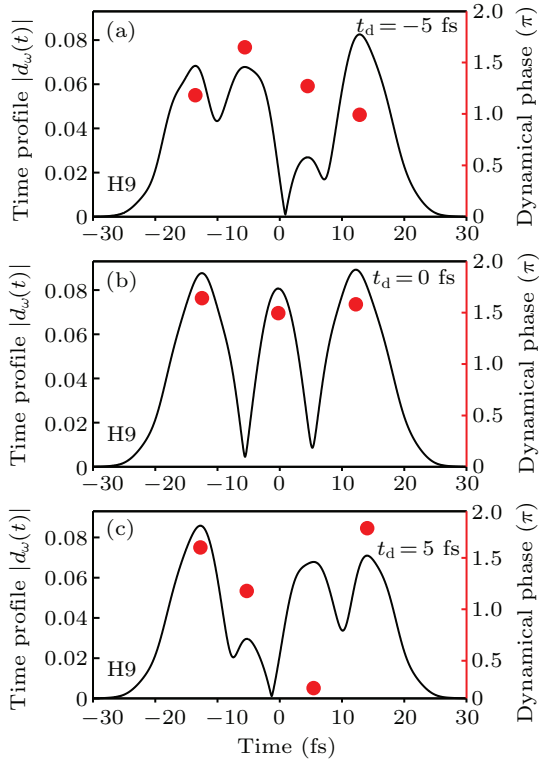


Fig. 5. The time profiles and dynamic phases of the 9th harmonic (H9) obtained from cross sections of the time-frequency spectrum in Fig. 4: (a) $t_d = -5$ fs, (b) $t_d = 0$ fs, (c) $t_d = 5$ fs. The red dots indicate the corresponding dynamic phases.

To discuss more detailed spectral and temporal structures in the high-harmonic orders for the different time delays, a representative time profile for the 9th harmonic (H9) obtained from cross sections of the time-frequency spectrum in Fig. 4 is shown in Figs. 5(a)–5(c). Note that the "dynamical phases" $\theta(t_q)$ (denoted by red dots) obtained from the wavelet transform of the intra-conduction band current are also presented. The dynamical phases $\theta(t_q)$ at the instant t_q can be calculated by $d_\omega(t) = |d_\omega(t_q)|\,\mathrm{e}^{-\mathrm{i}S(t_q)}$, where $S(t_q) = \omega t_q + \theta(t_q)$. The dynamical phases of the different time delays show different current trends. As is shown, the time profiles at $t_d = 0$ fs show a relatively smooth and continuous variation as a function of time, mimicking that of the driving laser pulse, this result is similar to the atomic case. Particularly, the dynamical phase is almost a constant. For the case of the time delay $t_d = -5$ fs and $t_d = 5$ fs, the time profiles show the fast-burst structure, and the dynamical phases also show some distinct changes. The HHG emission decreases obviously at the side of the subcycle laser pulse. It is in good agreement with the results shown in Fig. 4.

3.1.2. Evolution of oscillation structures in momentum space

As discussed above, we have presented the HHG oscillation structures in the crystal driven by an MIR and subcycle laser pulse with a time delay, and have discussed the spectral and temporal features of oscillation structures using time-frequency analysis of wavelet transform. We know that the electron is a free particle in the crystal. Namely, the interaction between the electron and lattice potential is implicitly considered by using crystal momentum instead of true momentum. This is mathematically reasonable since the crystal momentum operator, as the translation operator with translation distance, has the infinite lattice constant, which commutes with the field-free Hamiltonian, and thus shares the eigenstates. Next, we extend an acceleration theorem for the description of the evolution of oscillation structures in momentum space. This method involves a definition of the time-dependent crystal momentum $k(t)$:

$$\begin{aligned} k(t) &= \int_{\mathrm{BZ}} k f(k,t)\,\mathrm{d}k \\ &= \int_{\mathrm{BZ}} k\left[\int_{t_0}^{t} \frac{\mathrm{d}f(k,\tau)}{\mathrm{d}\tau}\,\mathrm{d}\tau\right]\mathrm{d}k \\ &= \frac{q}{\hbar}\int_{t_0}^{t} E(\tau)\,\mathrm{d}\tau, \end{aligned} \tag{21}$$

where $f(k,t)$ is the probability density distribution and $E(\tau)$ is the electric field at time t. As a result, using crystal momentum is somewhat like handling the problem in the frame rotating with the field-free Hamiltonian, and thereby the effect of lattice force, which is a term inside the field-free Hamiltonian, is implicitly considered and vanished. Therefore, the contribution of the radiation can be defined as an evaluation of group acceleration $a_g(k_c,t)$,

$$a_g(k_c,t) = \frac{q}{\hbar^2}\frac{\partial^2 \varepsilon(k_c)}{\partial k_c^2} E(t). \tag{22}$$

Notice that, unlike the group velocity, this group acceleration depends on both crystal momentum and time. We assume that the probability density in crystal momentum space is a narrow Gaussian distribution. Figure 6 shows the particle moves in the band along its trajectory, which is represented by the red curve. The effective mass is represented by the size of the ball and depends on the changes of the energy band. The color density indicates the radiation intensity determined by the effective mass and the intensity of the laser field. The charged particle with effective mass is pushed by the laser field force and starts to move in the band. It is easier to accelerate under the action of a laser pulse if the effective mass of a charged particle is relatively small, leading to higher radiation intensity. Furthermore, when the laser pushing force is so strong, the carrier can also produce strong radiation for a certain effective mass, since the larger laser force means that the charged particle is pushed or accelerated more strongly. This implies that the charged particle can produce strong radiation, because of a small effective mass of the carriers or the strong laser force enough to avoid considering its effective mass, when it happens to be at the position of the band structure. However, at those band positions marked by the blue ball, the carriers are essentially not radiated due to the larger effective mass of the carriers.

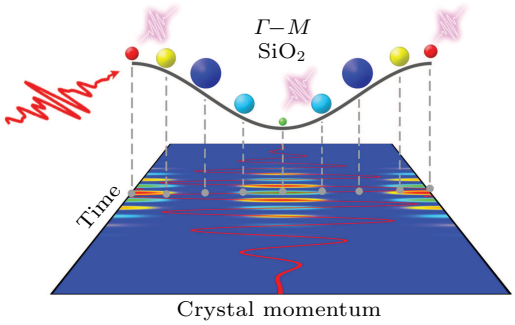


Fig. 6. Schematic diagram depicting the relation of effective mass and the position of the particles in intra-band HHG of crystals. The result shows how the effective mass changes at different positions of the band. The particle is depicted as a ball, and it can be defined by calculating the absolute value of effective mass. The band used here is a simple cosine model band. The red curve is the trajectory of the particle in the crystal momentum space. The background represents various light emissions.

In Figs. 7(a), 7(b), and 7(c), the detailed radiation distribution in crystal momentum space is presented as a function of the time delay $t_d = -5$ fs, $t_d = 0$ fs, and $t_d = 5$ fs, respectively. It is very clearly seen that there is no emission in blue color regions and have the strong emission in red and green colors indicated. The red and green regions are called positive and negative emission regions. It is important in the sense of emission with polarization in direction of the positive and negative direction. Different time delays have different emission conditions, and the emission intensity varies obviously with time delay t_d. By comparing the radiation intensity at the center of the Brillouin zone, we find that the effects of the few-cycle laser change the radiation interval and the radiation intensity in the time domain. This result is in good agreement with the spectral and temporal features of oscillation structures discussed above.

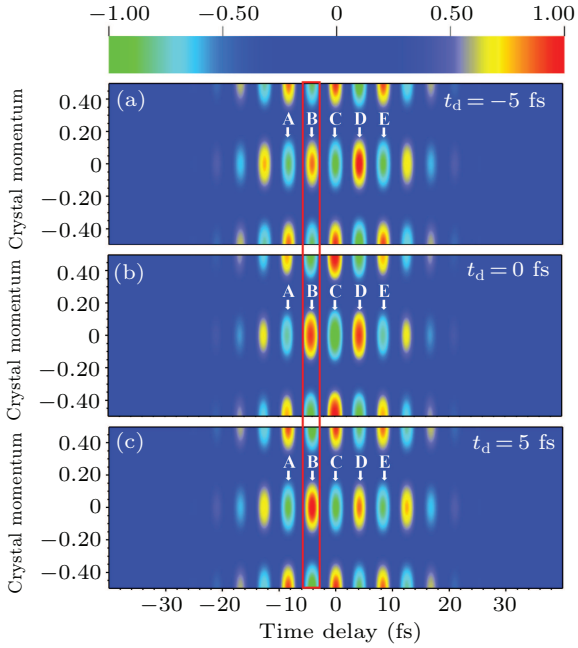


Fig. 7. Distribution of the emission intensity of the HHG in the crystal: (a) $t_d = -5$ fs, (b) $t_d = 0$ fs, (c) $t_d = 5$ fs, respectively. The laser parameters used are the same as those in Fig. 3. The red box indicates that the radiation intensity varies with the time delay.

3.2. Laser-induced HHG oscillation structure in multi-band model

Based on the above discussion, the same scheme can be extended for probing subcycle spectral structures and dynamics from the practically mixed intra- and inter-band crystalline HHG spectrum. A linearly polarized laser field is considered to propagate through the crystal along the optical axis in the simulation. The laser-crystal interaction is simplified in one dimension along the laser polarization. The harmonic spectra can be obtained by the Fourier transform of the microscopic current. In Fig. 8, we give the HHG spectra of the current calculated by solving the TDSE in velocity gauge. We have used 3 and 51 Bloch states in our expansion of wave function, which means that 3 and 51 bands are included in the calculations for each k value, respectively. The second band has the deepest bound energy, so we choose it as the initially populated valence band. Based on the HHG obtained by the numerically Bloch basis, we have used the subcycle laser field as the previous one in the first subsection and given oscillation structures in the multi-band model in Fig. 9.

When we use 3 band Bloch states in our expansion of wave function, the primary plateau is due to transitions between the valence band and the lowest conduction band. The oscillation structures of HHG are more complex, but variation trends are basically consistent with the results of our

single-band model on the whole. In particular, we can observe significant enhancement and suppression of the HHG either in single-band or multi-band crystal systems at three specific time delays. Then we have compared the results of 51 Bloch states in expansion of wave function in Fig. 10, whereas the secondary plateau and more generally higher frequencies in the spectrum are due to contributions from higher-lying bands. The same conclusion has been confirmed under these different conditions.

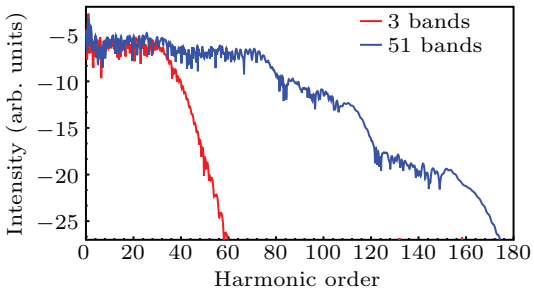


Fig. 8. High-harmonic spectra calculated by solving the TDSE based on Bloch state basis in velocity gauge.

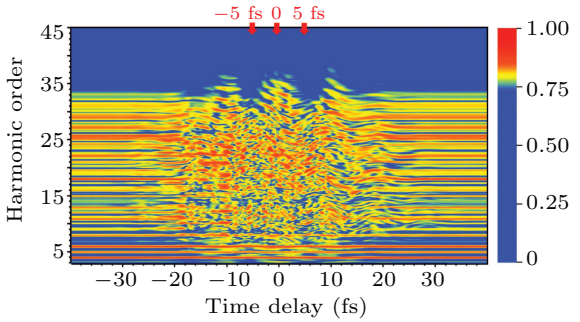


Fig. 9. HHG spectra as a function of the time delay between MIR and subcycle laser pulse in 3 bands model.

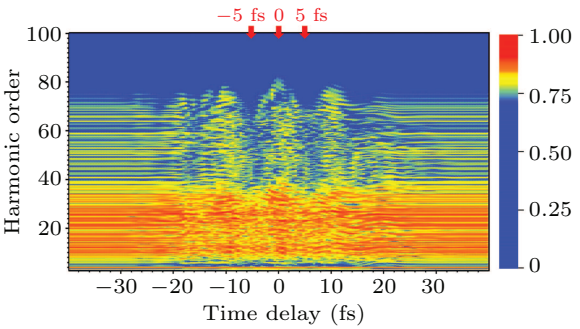


Fig. 10. HHG spectra as a function of the time delay between MIR and subcycle laser pulse in 51 bands model.

4. Conclusion

In summary, we have systematically studied oscillation structures of HHG and the carrier dynamics of the HHG in mid-infrared laser fields subject to excitation by a subcycle laser pulse with a time delay. However, it is complex to directly analyze the HHG spectrum from the mixed intra- and inter-band crystals because of multi-band contributions in crystals. Thus, it is significant to firstly explore the intra-band carrier contributions for us to understand the individual spectra features in crystals. We focus on two aspects. One is the emission characteristics of the time-frequency spectrum of the intra-band HHG, the other is the dynamical origin of the intra-band HHG in the crystal momentum. To well understand the dynamical mechanism of the spectrum oscillation structures of subcycle intra-conduction band, we adopt an acceleration theorem for the description of the evolution of oscillation structures in momentum space, and the emission dynamics of the intra-band HHG generated by the MIR and a subcycle laser pulse with a time delay are clarified. Furthermore, to a comprehensive understanding of subcycle spectral structures and dynamics of HHG processes in crystals, the same scheme has been extended for probing the oscillation structures of multi-band from the practically mixed intra- and inter-band crystalline HHG spectrum based on the Bloch state basis. The results indicate that the time-delay enhancement and suppression of the HHG related to subcycle pulse are observed at the given time delay in either single-band or multi-band crystal systems. Our result provides fresh insight to understand the crystal HHG processes excited by the sub-femtosecond pulse.

Acknowledgements

Project supported by the National Natural Science Foundation of China (Grant Nos. 12074239 and 91850209), the Natural Science Foundation of Guangdong Province, China (Grant Nos. 2020A1515010927 and 2020ST084), Department of Education of Guangdong Province, China (Grant Nos. 2019KTSCX038 and 2020KCXTD012), Shantou University (Grant No. NTF18030), the Natural Science basic Research Program of Shaanxi Province, China (Grant No. 2022JM-015), and Scientific Research Foundation of SUST (Grant No. 2017BJ-30).

References

[1] Corkum P B 1993 *Phys. Rev. Lett.* **71** 1994
[2] Paul A, Bartels R A, Tobey R, Green H, Weiman S, Christov I, Murnane M, Kapteyn H and Backus S 2003 *Nature* **421** 51
[3] Corkum P B and Krausz F 2007 *Nat. Phys.* **3** 381
[4] He L, Lan P, Le A T, Wang B, Zhu X, Lu P and Lin C D 2018 *Phys. Rev. Lett.* **121** 163201
[5] Li Y, Sato T and Ishikawa K L 2019 *Phys. Rev. A* **99** 043401
[6] Xiao F, Fan X, Wang L, Zhang D W, Wu J H, Wang X W and Zhao Z X 2020 *Chin. Phys. Lett.* **37** 114202
[7] Zhang J, Hua L Q, Chen Z, Zhu M F, Gong C and Liu X J 2020 *Chin. Phys. Lett.* **37** 124203
[8] Wang X Z, Wang Z H, Wang Y Y, Zhang X, Song J J and Wei Z Y 2021 *Chin. Phys. Lett.* **38** 074202
[9] Li W K, Lei Y, Li X, Yang T, Du M, Jiang Y, Li J L, Luo S Z, Liu A H, He L H, Ma P, Zhang D D and Ding D J 2021 *Chin. Phys. Lett.* **38** 053202
[10] Li F, Yang Y J, Chen J, Liu X J, Wei Z Y and Wang B B 2020 *Chin. Phys. Lett.* **37** 113201
[11] Itatani J, Levesque J, Zeidler D, Niikura H, Pépin H, Kieffer J C, Corkum P B and Villeneuve D M 2004 *Nature* **432** 867

[12] Zhai C, Zhu X, Lan P, Wang F, He L, Shi W, Li Y, Li M, Zhang Q and Lu P 2019 *Phys. Rev. A* **95** 033420

[13] Ghimire S, Ndabashimiye G, DiChiara A D, Sistrunk E, Stockman M I, Agostini P, DiMauro L F and Reis D A 2014 *J. Phys. B: At. Mol. Opt. Phys.* **47** 204030

[14] Vampa G and Brabec T 2017 *J. Phys. B: At. Mol. Opt. Phys.* **50** 083001

[15] Kruchinin S Y, Krausz F and Yakovlev V S 2018 *Rev. Mod. Phys.* **90** 021002

[16] Higuchi T, Stockman M I and Hommelhoff P 2014 *Phys. Rev. Lett.* **113** 213901

[17] Mrudul M S, Pattanayak A, Ivanov M and Dixit G 2019 *Phys. Rev. A* **100** 043420

[18] Ghimire S, DiChiara A D, Sistrunk E, Agostini P, DiMauro L F and Reis D A 2011 *Nat. Phys.* **7** 138

[19] Luu T T, Garg M, Kruchinin S Y, Moulet A, Hassan M T and Goulielmakis E 2015 *Nature* **521** 498

[20] Garg M, Zhan M, Luu T T, Lakhotia H, Klostermann T, Guggenmos A and Goulielmakis E 2016 *Nature* **538** 359

[21] Garg M, Kim H Y and Goulielmakis 2018 *Nat. Photon.* **12** 291

[22] Ghimire S and Reis D A 2019 *Nat. Phys.* **15** 10

[23] Guan Z, Wang G L, Zhang L, Jiao Z H and Zhao S F 2020 *Chin. Phys. Lett.* **38** 054201

[24] Schubert O, Hohenleutner M, Langer F, Urbanek B, Lange C, Huttner U, Golde D, Meier T, Kira M, Koch S W and Huber R 2014 *Nat. Photon.* **8** 119

[25] Vampa G, McDonald C R, Orlando G, Corkum P B and Brabec T 2015 *Phys. Rev. B* **91** 064302

[26] Kemper A F, Moritz B, Freericks J K and Devereaux T P 2013 *New J. Phys.* **15** 023003

[27] Fu S L, Feng Y K, Li J B, Yue S J, Zhang X, Hu B T and Du H C 2020 *Phys. Rev. A* **101** 023402

[28] Wu M, Ghimire S, Reis D A, Schafer K J and Gaarde M B 2015 *Phys. Rev. A* **91** 043839

[29] Li J B, Zhang X, Yue S J, Wu H M, Hu B T and Du H C 2017 *Opt. Express* **25** 18603

[30] Chen J G, Yang Y J, Chen J and Wang B B 2015 *Phys. Rev. A* **91** 043403

[31] Wang S, Zhu Z Y, Zhang Y Z, Yan T M and Jiang Y H 2020 *Chin. Phys. Lett.* **38** 013401

[32] Chini M, Wang X, Cheng Y, Wu Y, Zhao D, Telnov D A, Chu S I and Chang Z H 2013 *Sci. Rep.* **3** 1105

[33] Chen S, Bell M J, Beck A R, Mashiko H, Wu M, Pfeiffer A N, Gaarde M B, Neumark D M, Leone S R and Schafer K J 2012 *Phys. Rev. A* **86** 063408

[34] Heslar J, Telnov D A and Chu S I 2014 *Phys. Rev. A* **89** 052517

[35] Heslar J, Telnov D A and Chu S I 2015 *Phys. Rev. A* **91** 023420

[36] Zhao Y T, Jiang S C, Zhao X, Chen J G and Yang Y J 2020 *Opt. Lett.* **45** 2874

[37] Mücke O D 2011 *Phys. Rev. B* **84** 081202(R)

[38] Golde D, Meier T and Koch S W 2008 *Phys. Rev. B* **77** 075330

[39] Korbman M, Kruchinin S Y and Yakovlev V S 2013 *New J. Phys.* **15** 013006

[40] Chini M, Zhao B, Wang H, Cheng Y, Hu S X and Chang Z H 2012 *Phys. Rev. Lett.* **109** 073601

[41] Gilbertson S, Chini M, Feng X, Khan S, Wu Y and Chang Z H 2010 *Phys. Rev. Lett.* **105** 263003

[42] Wang H, Chini M, Chen S, Zhang C H, He F, Cheng Y, Wu Y, Thumm U and Chang Z H 2010 *Phys. Rev. Lett.* **105** 143002

[43] Tamaya T and Kato T 2019 *Phys. Rev. B* **100** 081203(R)